Supporting Information:

Side-chain torsional dynamics strongly influence charge transport in organic semiconductors

Peter A. Banks, Adam M. Dyer, Adam C. Whalley, and Michael T. Ruggiero*

Department of Chemistry, University of Vermont, 82 University Place, Burlington, Vermont 05405, United States of America

E-mail: Michael.Ruggiero@uvm.edu

Synthetic Methods

3,8-Bis(5-hexyl-2-thienyl)dimethoxy[1]benzothieno[3,2-b][1]benzothiophene (C6-DT-BTBT): 3,8-TfO-BTBT (0.100g, 0.1864 mmol), K_2CO_3 (0.155 g, 1.1185 mmol), 2-(5-hexyl-2-thienyl)-4,4,5,5-tetramethyl1,3,2-dioxaborolane (HT-Bpin) (0.559 g, 0.165 mmol), H_2O (0.56 mL), and THF (6 mL) were added to flame dried round bottom flask equipped with a reflux condenser and degassed. Synthetic precursors 3,8-TfO-BTBT and HT-Bpin were prepared following reported procedures.[S1,S2] $Pd(PPh_3)_4$ (0.011g, 0.0093 mmol) was added and the reaction was refluxed for 12 hours. After it was cooled to room temperature, quenched with NH_4Cl saturated solution, extracted with EtOAc and CH_2Cl_2, it was recrystallized from $CHCl_3$/MeOH several times to afford C6-DT-BTBT as a colorless solid (0.080 g, 0.1398 mmol, 75%). ^{1}H NMR (500 MHz, $CDCl_3$) δ = 8.02 (d, J = 1.6 Hz, 2H), 7.89 (d, J = 8.5 Hz, 2H), 7.63 (dd, J = 8.4, 1.7 Hz, 2H), 7.24 (d, J = 3.5 Hz, 2H), 6.80 (d, J = 3.5 Hz, 2H),

2.86 (t, J = 7.6 Hz, 4H), 1.73 (p, J = 7.5 Hz, 4H), 1.42 (m, 4H), 1.34 (m, 8H), 0.91 (m, Hz, 6H) ppm. ^{13}C NMR (126 MHz, CDCl$_3$) δ = 146.09, 141.21, 140.71, 134.03, 133.56, 132.13, 125.16, 124.27, 123.17, 123.13, 118.13, 31.67, 31.61, 30.33, 28.81, 22.60, 14.10 ppm. HRMS ESI [M +] calcd. for C$_{34}$H$_{36}$S$_4$: 572.1700; found: 527.1708.

Characterization

^{1}H NMR spectra were collected on a Bruker Ascend 500 MHz spectrometer (Bruker, Billerica, MA). ^{13}C NMR spectra were collected on a Bruker Ascend 500 MHz spectrometer at 125 MHz. All spectra were calibrated to an internal tetramethylsilane (TMS) standard.High-resolution mass spectra (HRMS) were recorded on a Waters Xevo G2-XS LCMS-QTOF spectrometer (Waters Corp., Milford, MA).
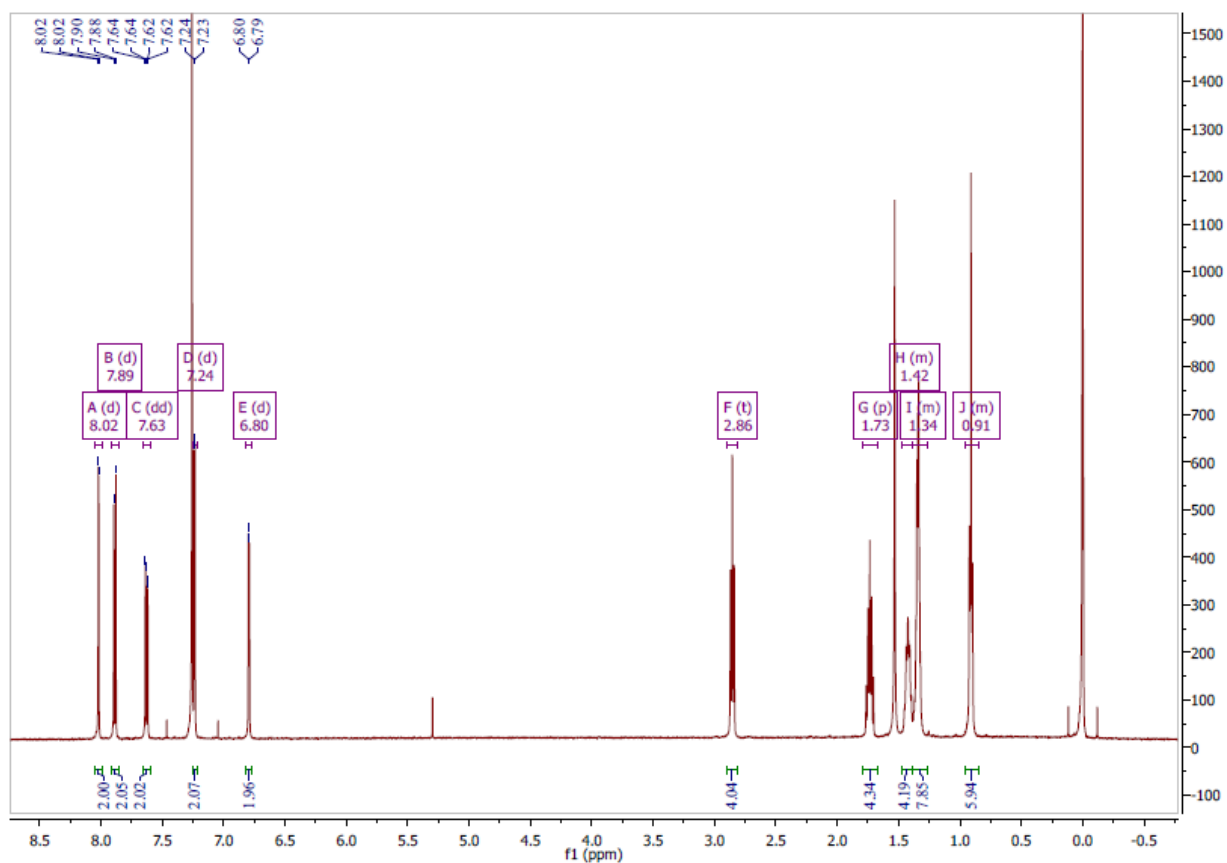

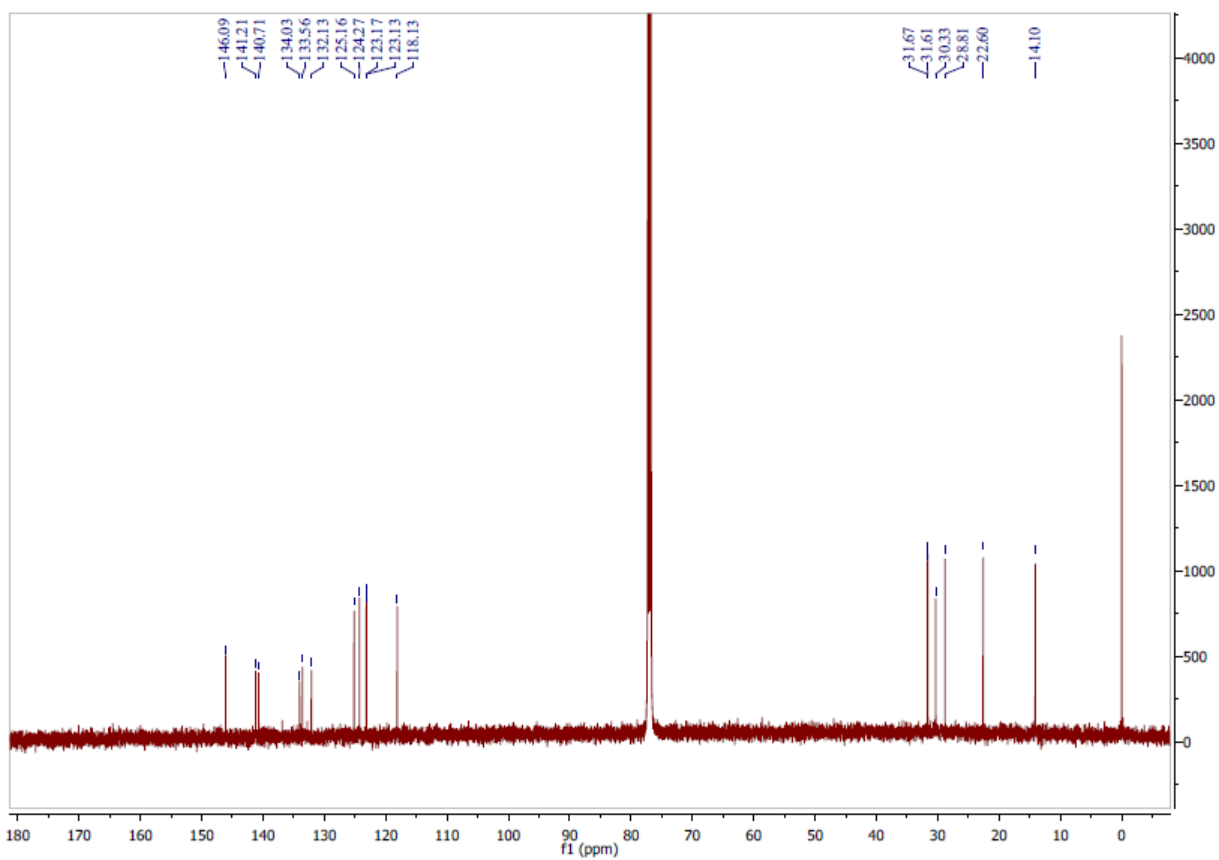**Figure S1:** ^{1}H NMR spectrum of C6-DT-BTBT.

Figure S2: ^{13}C NMR spectrum of C6-DT-BTBT.

AD-3,8-BTBT final pos ESI Xevo 30 (0.570)

1: TOF MS ES+
7.55e5

572.1708
755343

AD 3,8-BTBT final pos ESI cmpd#1 M⁺

Theoretical mass:	572.1700
Measured mass:	572.1708
Delta in ppm:	1.398
Delta in mmu:	0.800
acceptable in mmu:	3.000
acceptable in ppm:	5.243

573.1754
366223

572.3580
93294

572.5211
77971

572.6943
62072

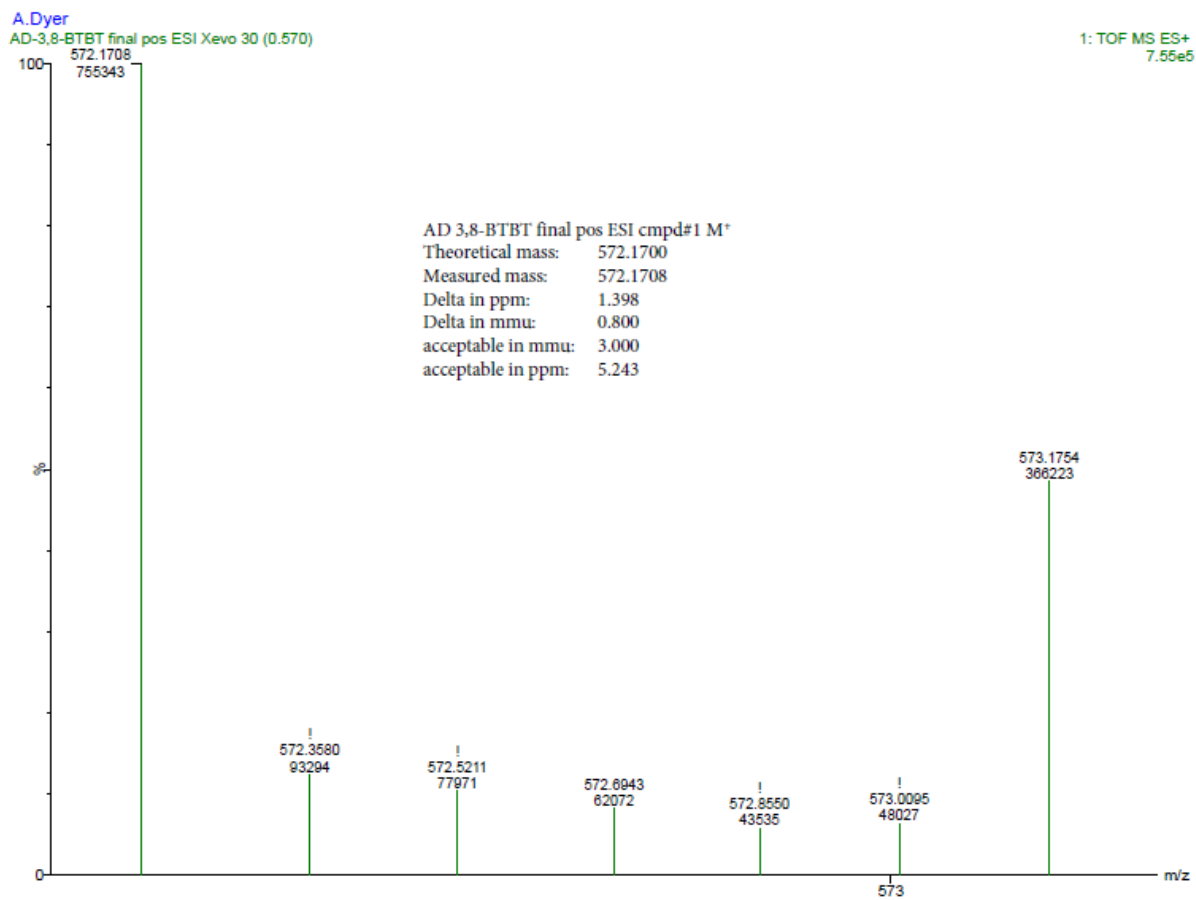572.8550
43535

573.0095
48027

m/z

573

Figure S3: High resolution mass spectrum of C6-DT-BTBT.

Single-Crystal Diffraction Methods

Diffraction experiments were carried out using a Bruker AXS single-crystal diffractometer, equipped with a monochromatic Mo K$_\alpha$ ($\lambda = 0.70926$Å) radiation source and SMART APEX CCD area-detector. Absorption effect corrections were carried out using the multiscan method (SADABS), and structural solutions were obtained with direct methods using the SHEXL refinement program.[S3,S4] Non-hydrogen atoms were refined anisotropically, followed by identification of all hydrogen atoms based on a residual electron density analysis. Subsequently, all atoms were then refined isotropically.

Theoretical Methods

Periodic Simulations

Solid-state DFT calculations of the investigated materials were carried out using the CRYSTAL17 package.[S5,S6] Geometric optimizations were performed upon crystalline structures derived from single crystal X-ray experiments, allowing all lattice vectors and atomic positions to fully relax with no restraints except the experimentally derived space group symmetry of the solid, yielding optimized structures that were achieved with a convergence criteria of 10^{-8} hartree. Brillouin zone sampling was performed using a Monkhorst-Pack scheme. Vibrational frequency analyses were performed within the harmonic approximation, calculating the numerically determined second derivatives of the potential energy surface using a two-point scheme to afford the mass-weighted Hessian matrix, which upon diagonalization yields Γ-point eigenvalues (vibrational transition frequencies) and eigenvectors (normal modes). Vibrational analysis employed an energy convergence criterion of 10^{-11} hartree.[S6–S8] All optimization and frequency simulations were performed using the double-ζ def2-SVP basis set, along with the PBE GGA density functional, corrected with Grimme's dispersion terms (D3) and becke-johnson damping functions.[S9–S13] Because of the ultrasoft nature of low-

frequency vibrations,[S14,S15] any vibrational mode predicted with a transition frequency less that $20\,\mathrm{cm}^{-1}$ was corrected through determination of the anharmonic potential of the normal mode, at which point the fundamental anharmonic transition frequency was calculated from the 1-D anharmonic oscillator Schrodinger equation, using a sixth-order polynomial fit of the newly determined potential energy surface.[S16] In these cases, the corrected anharmonic transition frequency was used for further analysis (*vide infra*).

Mode-resolved Electron-Phonon Couplings and Transfer Integral Fluctuations

The electronic structure of 2-D organic semiconductors was considered using the procedure of Girlando *et al.*,[S17,S18] using the tight binding model as a frame work with the corresponding Hamiltonian:

$$H = \sum_i \epsilon_i a_i^+ a_i + \sum_{i,j} J_{ij}(a_i^+ a_j + H.c.) \tag{1}$$

With energy of molecular site i ϵ_i, intermolecular transfer integral J_{ij}, and creation and annihilation operators a_i^+ and a_i. Intermolecular transfer integrals were calculated using the dimer projection approach,[S19,S20] carried out using single point energy calculations using the ORCA v4.0 code, using the def2-SVP basis set and the hybrid PBE0 density functional.[S13,S21,S22] Because these systems exhibit hole transport, transfer integrals were calculated as HOMO-HOMO matrix elements. Non-local electron phonon couplings (β_x) were calculated through finite displacement differentiation of the transfer integral J_{ij} about the equilibrium geometry along displacement of normal mode Q_k:

$$\beta_{x,k} = \left(\frac{\partial J_x}{\partial Q_k}\right)_0 \tag{2}$$

Transfer integral fluctuations σ are evaluated using the calculated non-local electron-phonon coupling $\beta_{x,k}$, and classical thermal vibrational amplitude σ_k^Q:

$$\sigma = \beta_{x,k}\, \sigma_k^Q \tag{3}$$

$$[\sigma_k^Q(T)]^2 = \frac{k_B T}{m_k \omega_k^2} \tag{4}$$

With Boltzmann constant K_B, temperature T evaluated at 298K, reduced mass of mode k m_k, and vibrational transition frequency ω_k. The total thermal disorder is determined from transfer integral fluctuations for each unique transfer integral in the unit cell, such that:

$$\sigma = \sqrt{\sigma_a^2 + \sigma_b^2 + \sigma_c^2} \tag{5}$$

Table S1: Identified unique transfer integrals for each of the investigated materials reported in meV.

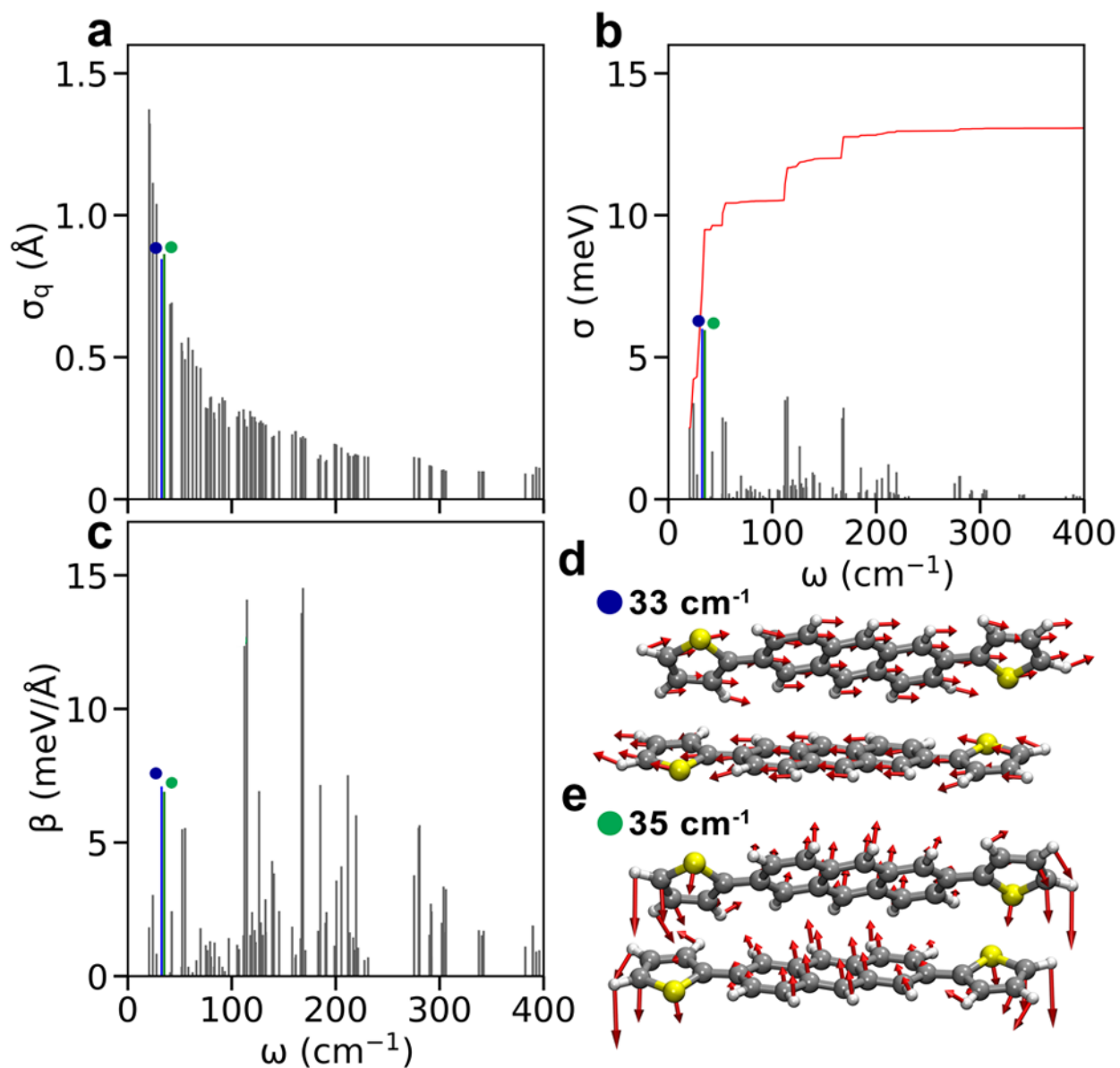|	J_a (meV)	J_b (meV)
DT-Ant	-30.355	60.076
C6-DT-BTBT	36.733	–
DT-P	127.499	-3.05549
DT-Pen	130.631	–

Figure S4: Results of the dimer projection analysis for DT-Ant. **a** Classical thermal vibrational vibrational amplitude, **b** non-local electron-phonon couplings, and **c** transfer integral fluctuations for each predicted vibrational mode, represented by vertical lines. **d** Molecular motions of modes that induce large transfer integral fluctuations, with transition frequencies $33\,\mathrm{cm}^{-1}$ and $35\,\mathrm{cm}^{-1}$, respectively, with red arrows illustrating atomic displacement. These modes are noted on **a-c** with blue and green circles, respectively.
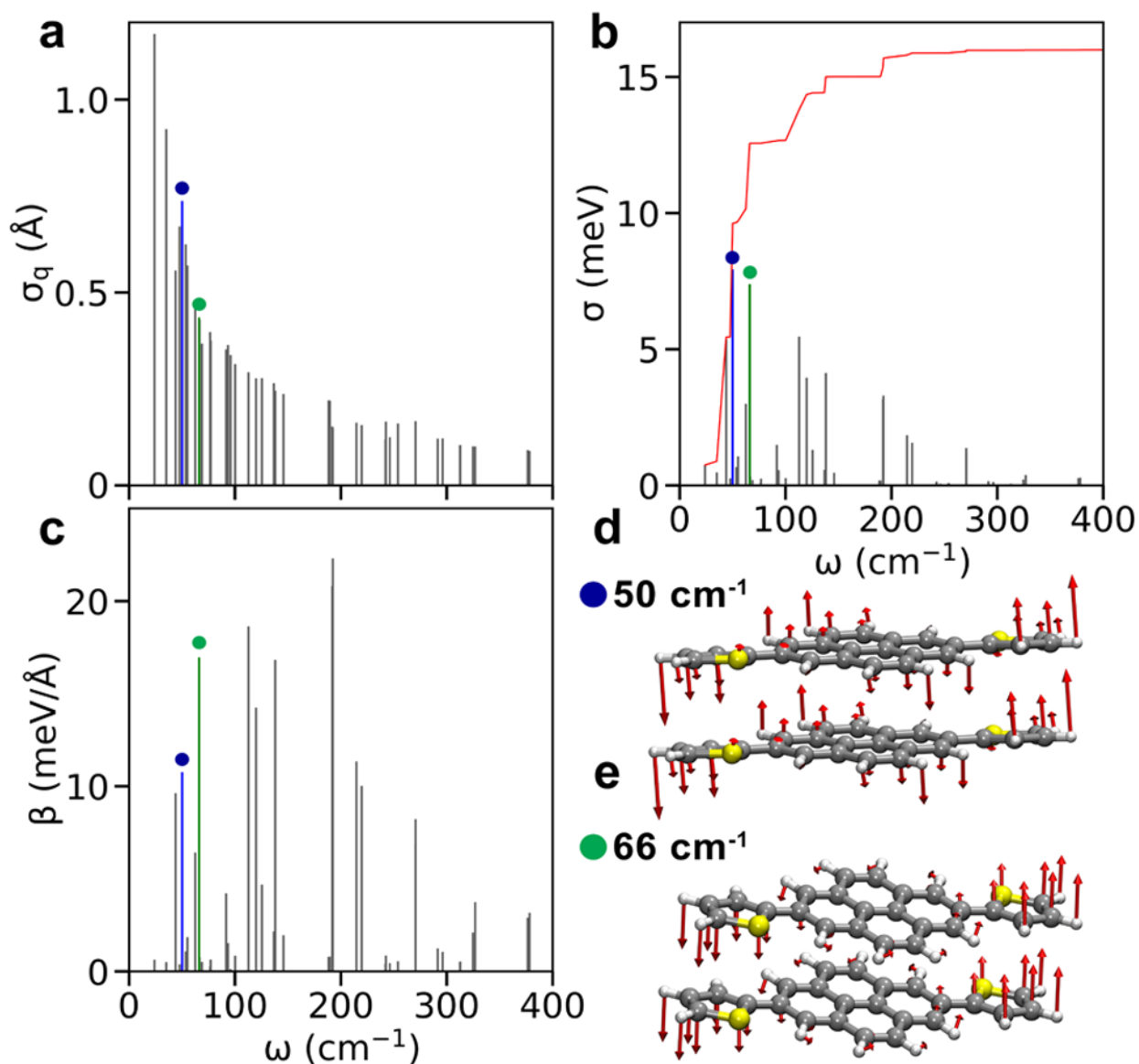
Figure S5: Results of the dimer projection analysis for DT-Ant. **a** Classical thermal vibrational vibrational amplitude, **b** non-local electron-phonon couplings, and **c** transfer integral fluctuations for each predicted vibrational mode, represented by vertical lines. **d** Molecular motions of modes that induce large transfer integral fluctuations, with transition frequencies $50\,\mathrm{cm}^{-1}$ and $66\,\mathrm{cm}^{-1}$, respectively, with red arrows illustrating atomic displacement. These modes are noted on **a-c** with blue and green circles, respectively.
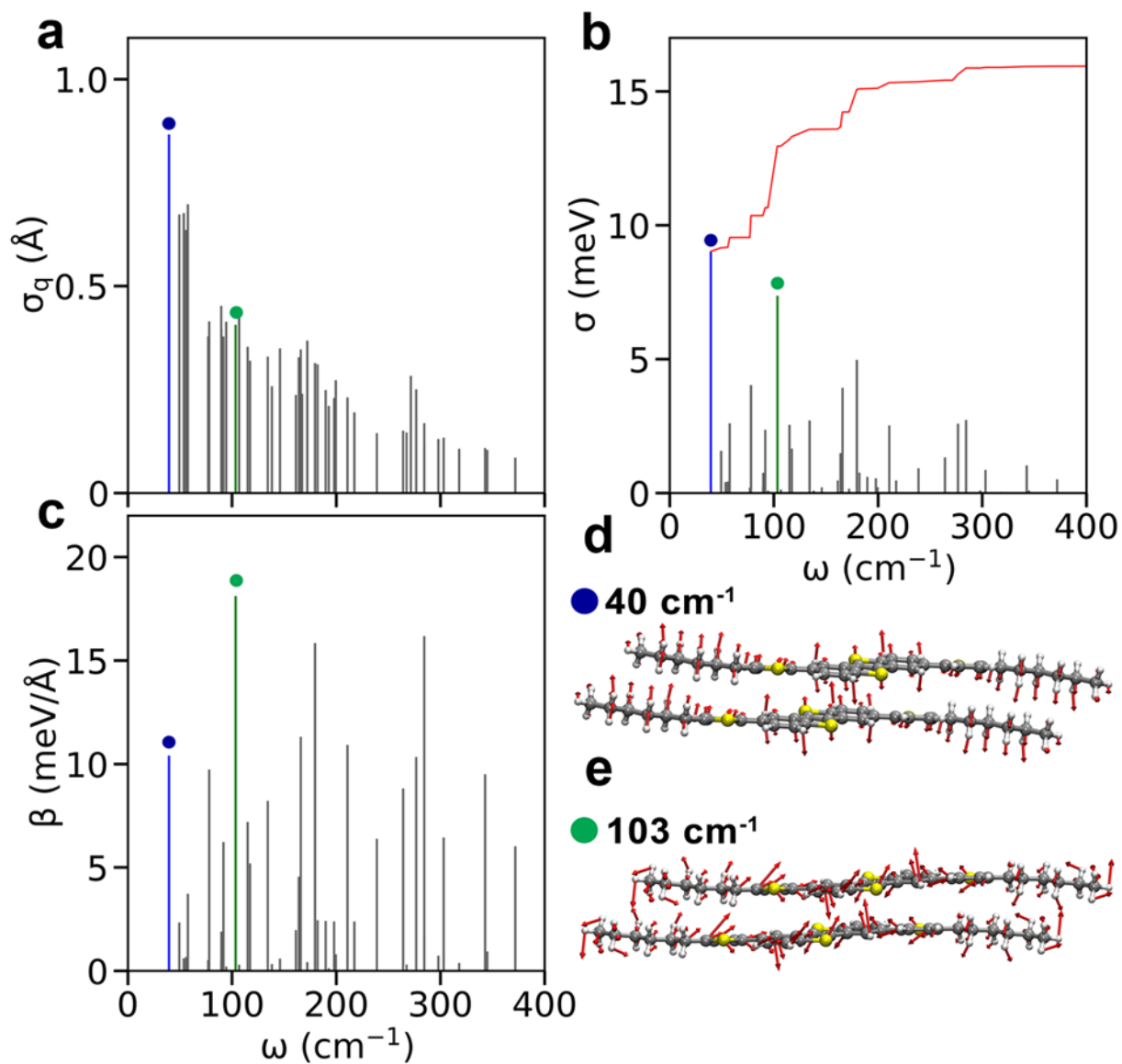
S-9

Figure S6: Results of the dimer projection analysis for C6-DT-BTBT. **a** Classical thermal vibrational vibrational amplitude, **b** non-local electron-phonon couplings, and **c** transfer integral fluctuations for each predicted vibrational mode, represented by vertical lines. **d** Molecular motions of modes that induce large transfer integral fluctuations, with transition frequencies $40\,cm^{-1}$ and $103\,cm^{-1}$, respectively, with red arrows illustrating atomic displacement. These modes are noted on **a-c** with blue and green circles, respectively.
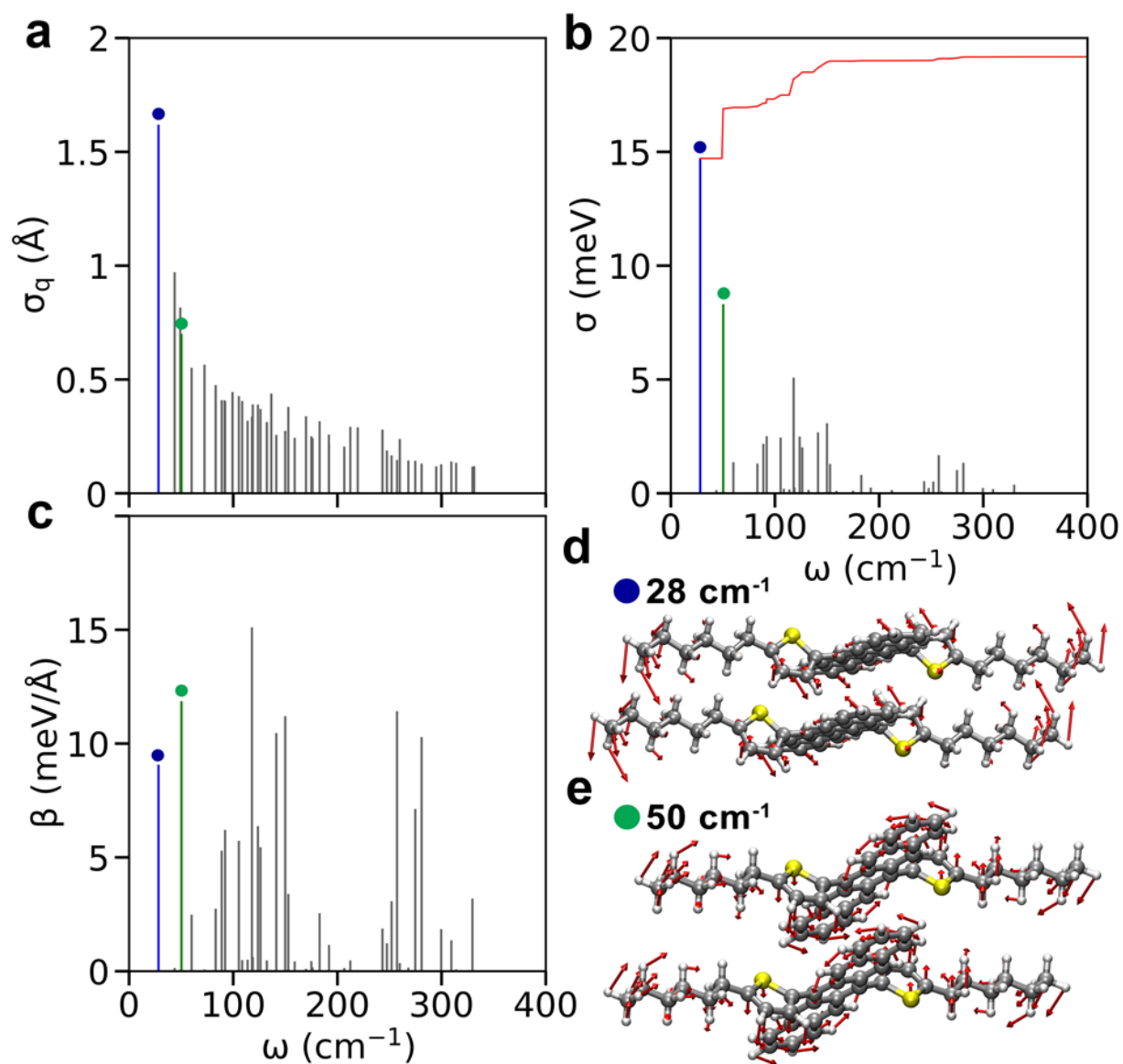
Figure S7: Results of the dimer projection analysis for DT-Pen. **a** Classical thermal vibrational vibrational amplitude, **b** non-local electron-phonon couplings, and **c** transfer integral fluctuations for each predicted vibrational mode, represented by vertical lines. **d** Molecular motions of modes that induce large transfer integral fluctuations, with transition frequencies $28\,\mathrm{cm^{-1}}$ and $50\,\mathrm{cm^{-1}}$, respectively, with red arrows illustrating atomic displacement. These modes are noted on **a-c** with blue and green circles, respectively.

References

(S1) Lee, C. H.; Plunkett, K. N. Orthogonal functionalization of cyclopenta[hi]aceanthrylenes. *Org. Let.*. **2013**, *15*, 1202–1205.

(S2) Dyer, A. M. Synthesis and Characterization of Highly Contorted Aromatics and Semiconducting Thioacenes. Ph.D. thesis, University of Vermont, 2021.

(S3) Sheldrick, G. M. *SADABS, program for empirical absorption correction of area detector data*; University of Göttingen, 1996.

(S4) Sheldrick, G. M. Crystal structure refinement with *SHELXL. Acta Crystallogr. C* **2015**, *71*, 3–8.

(S5) Erba, A.; Baima, J.; Bush, I.; Orlando, R.; Dovesi, R. Large-Scale Condensed Matter DFT Simulations: Performance and Capabilities of the CRYSTAL Code. *J. Chem. Theory Comput* **2017**, *13*, 5019–5027.

(S6) Dovesi, R.; Erba, A.; Orlando, R.; Zicovich-Wilson, C. M.; Civalleri, B.; Maschio, L.; Rérat, M.; Casassa, S.; Baima, J.; Salustro, S.; Kirtman, B. Quantum-mechanical condensed matter simulations with CRYSTAL. *WIREs Comput. Mol. Sci.* **2018**, *8*, e1360.

(S7) Dovesi, R.; Erba, A.; Orlando, R.; Zicovich-Wilson, C. M.; Civalleri, B.; Maschio, L.; Rérat, M.; Casassa, S.; Baima, J.; Salustro, S.; Kirtman, B. Quantum-mechanical condensed matter simulations with CRYSTAL. *Wiley Interdiscip. Rev. Comput. Mol. Sci.* **2018**, *8*, e1360.

(S8) Pascale, F.; Zicovich-Wilson, C. M.; López Gejo, F.; Civalleri, B.; Orlando, R.; Dovesi, R. The calculation of the vibrational frequencies of crystalline compounds and its implementation in the CRYSTAL code. *J. Comput. Chem.* **2004**, *25*, 888–897.

(S9) Perdew, J. P.; Burke, K.; Ernzerhof, M. Generalized gradient approximation made simple. *Phys. Rev. Lett.* **1996**, *77*, 3865–3868.

(S10) Smith, D. G.; Burns, L. A.; Patkowski, K.; Sherrill, C. D. Revised Damping Parameters for the D3 Dispersion Correction to Density Functional Theory. *J. Phys. Chem. Lett.* **2016**, *7*, 2197–2203.

(S11) Grimme, S.; Ehrlich, S.; Goerigk, L. Effect of the damping function in dispersion corrected density functional theory. *J. Comput. Chem.* **2011**, *32*, 1456–1465.

(S12) Grimme, S. Density functional theory with London dispersion corrections. *WIREs Comput. Mol. Sci.* **2011**, *1*, 211–228.

(S13) Weigend, F.; Ahlrichs, R. Balanced basis sets of split valence, triple zeta valence and quadruple zeta valence quality for H to Rn: Design and assessment of accuracy. *Phys. Chem. Chem. Phys.* **2005**, *7*, 3297–3305.

(S14) Schweicher, G.; D'Avino, G.; Ruggiero, M. T.; Harkin, D. J.; Broch, K.; Venkateshvaran, D.; Liu, G.; Richard, A.; Ruzié, C.; Armstrong, J.; Kennedy, A. R.; Shankland, K.; Takimiya, K.; Geerts, Y. H.; Zeitler, J. A.; Fratini, S.; Sirringhaus, H. Chasing the "Killer" Phonon Mode for the Rational Design of Low-Disorder, High-Mobility Molecular Semiconductors. *Adv. Mater.* **2019**, *31*, 1902407.

(S15) Otaki, T.; Terashige, T.; Tsurumi, J.; Miyamoto, T.; Kida, N.; Watanabe, S.; Okamoto, T.; Takeya, J.; Okamoto, H. Evaluations of nonlocal electron-phonon couplings in tetracene, rubrene, and C10-DNBDT-NW based on density functional theory. *Phys. Rev. B* **2020**, *102*, 245201.

(S16) Hutereau, M.; Banks, P. A.; Slater, B.; Zeitler, J. A.; Bond, A. D.; Ruggiero, M. T. Resolving Anharmonic Lattice Dynamics in Molecular Crystals with X-Ray Diffraction and Terahertz Spectroscopy. *Phys. Rev. Lett.* **2020**, *125*, 103001.

(S17) Girlando, A.; Grisanti, L.; Masino, M.; Bilotti, I.; Brillante, A.; Della Valle, R. G.; Venuti, E. Peierls and Holstein carrier-phonon coupling in crystalline rubrene. *Phys. Rev. B* **2010**, *82*, 035208.

(S18) Girlando, A.; Grisanti, L.; Masino, M.; Brillante, A.; Della Valle, R. G.; Venuti, E. Interaction of charge carriers with lattice and molecular phonons in crystalline pentacene. *J. Chem. Phys.* **2011**, *135*, 84701.

(S19) Valeev, E. F.; Coropceanu, V.; Da Silva Filho, D. A.; Salman, S.; Brédas, J. L. Effect of electronic polarization on charge-transport parameters in molecular organic semiconductors. *J. Am. Chem. Soc.* **2006**, *128*, 9882–9886.

(S20) Baumeier, B.; Kirkpatrick, J.; Andrienko, D. Density-functional based determination of intermolecular charge transfer properties for large-scale morphologies. *Phys. Chem. Chem. Phys.* **2010**, *12*, 11103–11113.

(S21) Neese, F. The ORCA program system. *WIREs Comput. Mol. Sci.* **2012**, *2*, 73–78.

(S22) Perdew, J. P.; Ernzerhof, M.; Burke, K. Rationale for mixing exact exchange with density functional approximations. *J. Chem. Phys.* **1996**, *105*, 9982.